

NEXAFS and FTIR-ATR Investigation of the Static and Dynamic Superhydrophobicity of Functionalized Titanium Dioxide Nanoparticle Coatings

Rajajeyaganthan Ramanathan and Daniel E. Weibel*

*Instituto de Química, Universidade Federal do Rio Grande do Sul (UFRGS),
Av. Bento Gonçalves 9500, CP 15003, 91501-970 Porto Alegre-RS, Brazil*

Superfícies super-hidrofóbicas com ângulos de contacto maiores ou iguais a 159° foram preparadas utilizando nanopartículas de dióxido de titânio e trimetoxipropil silano (TMPSi) em solventes aquosos ou não aquosos. A superfície super-hidrofóbica preparada em solvente aquoso mostrou uma histerese angular alta. Por outro lado, a superfície super-hidrofóbica preparada em solvente não aquoso teve uma histerese angular baixa e propriedades auto-limpantes. O uso da espectroscopia NEXAFS (*Near Edge X-ray Absorption Fine Structure*) é demonstrado e justificado no estudo de superfícies super-hidrofóbicas com a ajuda da espectroscopia no infravermelho com transformada de Fourier no modo de refletância total atenuada (FTIR-ATR). O presente estudo realça a importância da heterogeneidade química de uma superfície sobre as propriedades finais de uma superfície super-hidrofóbica. As propriedades autolimpantes de uma superfície super-hidrofóbica somente são obtidas com um completo recobrimento da superfície com TMPSi quando um solvente não aquoso é utilizado. Esse resultado é sustentado por dados detalhados de NEXAFS e FTIR-ATR.

Superhydrophobic surfaces with static water contact angles higher or equal to 159° were fabricated using titanium dioxide nanoparticles and trimethoxypropyl silane (TMPSi) in aqueous or non-aqueous solvents. The superhydrophobic surface fabricated in aqueous solvent showed high contact angle hysteresis. On the other hand, the superhydrophobic surface fabricated in non-aqueous solvent showed low contact angle hysteresis and self-cleaning properties. The application of near edge X-ray absorption fine structure (NEXAFS) spectroscopy in surface analysis of superhydrophobic surface is demonstrated and justified with the help of Fourier transform infrared spectroscopy by attenuated total reflectance (FTIR-ATR). The present work highlights the importance of chemical heterogeneity of the surface on the final properties of a superhydrophobic surface. The self cleaning superhydrophobic surface is obtained only with a complete coverage of the surface with TMPSi in a non-aqueous solvent. This finding is supported by detailed NEXAFS and FTIR-ATR data.

Keywords: superhydrophobic, titanium dioxide, NEXAFS, contact angle hysteresis

Introduction

When a liquid droplet contacts a solid surface, that droplet will either spread out on the surface or remain as a droplet depending on the surface characteristics. If the water contact angle (CA) is larger than 150°, the surface is defined as superhydrophobic. In the last decade, extensive studies have been carried out to analyze such superhydrophobic surfaces revealing the importance of surface roughness and chemical morphology.¹⁻⁸ There are two possible wetting states on rough surfaces: the Wenzel⁹ which is a homogeneous state and the

Cassie and Baxter¹⁰ that is a composite state. In the Wenzel state, the water droplets pin the surface in a wet-contact mode without any movement, even if the surface is fitted to a vertical position or turned upside down. In the Cassie state, the water droplet adopts a non-wet contact mode on the solid surface and can easily roll off due to their low water adhesion. The contact angle hysteresis (CAH), which is the difference between the contact angle at the increased droplet volume (θ_A) and the contact angle at the decreased droplet volume (θ_B), for a droplet on these superhydrophobic surfaces has a value lower than ca. 10°. Superhydrophobicity with low hysteresis promises plenty of valuable usages in practice, such as self-cleaning,¹¹ anti-sticking¹² and anti-contamination.¹

*e-mail: danielw@iq.ufrgs.br

Additionally, a transitory state between the Wenzel and Cassie states known as transition or metastable state, in which a water droplet can transit from a composite to a fully wetted state upon external disturbances, also exists. In this metastable state, an energy barrier between those two states which, can be overcome by external disturbances, was proposed.^{13,14} A new superhydrophobic state called the Gecko state prepared with superhydrophobic polystyrene nanotubes¹⁵ with high adhesive force mimicking the Gecko feet was also proposed by Wang *et al.*¹⁶ The states of a superhydrophobic surface are also a subject of controversy based on contact area, triple phase liquid/air/solid contact line and which state pertains to different circumstances.¹⁶⁻²⁰

A lotus leaf is the prototype of a superhydrophobic surface, but there is another one called the rose petal effect, which is a superhydrophobic state with high CAH. In the superhydrophobic surface of a rose petal (*rosea* Rehd), a water droplet cannot roll off even when the petal is turned upside down.²¹ The high hysteresis of the rose petal is explained by the different designs in the surface hierarchical micro and nanostructures where the water droplet can impregnate the microstructure and partially penetrates into the nanostructure. This intermediate state is referred as the Cassie impregnating wetting state.^{21,22} Wetability and in particular the hysteresis on superhydrophobic surfaces are mainly ruled by the surface geometrical structure and surface composition. CAH is influenced by thermodynamic and kinetic factors such as surface structure and heterogeneity, chemical heterogeneity, triple phase contact line, liquid penetration, surface mobility, surface defects, etc.^{23,24}

The use of synchrotron radiation sources presents new opportunities to apply X-ray absorption spectroscopy to a variety of analytical problems. Electronic and structural properties are studied by many tools and techniques developed over the last century. Synchrotron based spectroscopic techniques have contributed significantly to understand the microscopic properties in the last decades. Among synchrotron-based spectroscopic techniques, near edge X-ray absorption fine structure (NEXAFS) spectroscopy, also called XANES (X-ray absorption near edge structure), probes the absorption of electromagnetic radiation by excitation of core electrons into unoccupied bound or continuum states, which in turn are helpful to study the electronic and the structural properties of materials. NEXAFS spectroscopy uses tunable, polarized X-rays from a synchrotron source to determine which bonds are present on the surface as well as their orientation.²⁵⁻²⁷ The X-rays used in NEXAFS spectroscopy excite a core electron into an empty molecular orbital,

leaving a hole in the core shell. This hole is filled by an electron from a higher energy level and an Auger electron is emitted. The number of Auger electrons that are detected for a specific given X-ray energy supplies information about the number of core-holes that are created and therefore the transition that is occurring. NEXAFS has been successfully utilized for a wide range of adsorbate system, in which the spectroscopy has provided useful information contributing to the understanding of both adsorption geometries and surface chemical bond. NEXAFS spectroscopy is precisely in the soft X-ray spectral region where sharp core levels are found for S, C, N, Ti, O and F elements occurring in materials. NEXAFS selects a specific atomic species through its K-edge and probes its bonds to intra-molecular and extra-molecular (surface atoms) neighbors. By comparing the spectra for free and chemisorbed molecules, NEXAFS spectroscopy can also reveal which orbitals are involved in the chemisorption bond.²⁶ In NEXAFS spectroscopy, the signal obtained by electron yield detection mode is surface sensitive when compared to fluorescence yield (bulk sensitive) and the information depth of NEXAFS spectroscopy in total electron yield mode is between 20 and 40 Å.²⁸

Our group has recently shown that a very simple and inexpensive method to fabricate superhydrophobic surfaces using functionalized TiO₂ nanoparticles with different liquid-solid adhesion properties can be prepared using lower alkyl chain silane in different solvents.²⁹ The difference in hysteresis of the superhydrophobic surfaces prepared was explained by the size difference of hierarchical micro and nanostructures together with different chemical surface properties. In particular, a novel liquid-solid adhesive behavior was found in coatings prepared in water solutions compared to xylene solutions. Based on X-ray photoelectron spectroscopy (XPS) data, the results were explained by the presence of Ti-OH groups on titanium dioxide left uncovered by oligomeric siloxanols formed in aqueous solution during aging. The present work is a step forward in the comprehension on the chemical aspects controlling the dynamic of a water drop on a superhydrophobic surface. NEXAFS and FTIR-ATR data of superhydrophobic surface fabricated using titanium dioxide and short alkyl chain silane (trimethoxypropyl silane) in aqueous (water/ethanol) and non-aqueous (xylene) solvent were investigated. NEXAFS spectroscopy was *in situ* applied to monitor the surface composition and chemical state of the superhydrophobic surfaces. From the data obtained, the interactions of the water drop on the different TiO₂ functionalized surfaces are elucidated.

Experimental

Chemicals

Trimethoxypropyl silane (TMPSi) of purity 97% was obtained from Sigma-Aldrich (Brazil). Xylene (mixture of isomers) was purchased from Merck (Brazil). Titanium dioxide nanoparticle powder, AEROXIDE[®] TiO₂-P25, was received from Degussa Corporation (Evonik, Brazil) and used without any further treatment.

Nanoparticle functionalization

TiO₂ nanoparticle functionalization was carried out following the procedure previously published.²⁹ Briefly, diluted TMPSi-aqueous solution (5/95% v/v, TMPSi/water) was prepared by premixing TMPSi and ethanol in equal amounts in deionized water. The TMPSi-aqueous solution was stirred for few minutes and then aged until the solution became hazy. After aging, a TMPSi-aqueous solution was stirred with 0.3 g of titanium dioxide for a few minutes. The stirred solution was then casted on 10 mm × 10 mm stainless steel plates, placed in Petri dish and left inside the oven at a moderate temperature (about 100 °C) to increase the condensation reaction rates. For comparison with the titanium dioxide film prepared from TMPSi-aqueous solution (ATMPSi), another titanium dioxide film was prepared using the same concentration of titanium dioxide and TMPSi in xylene solvent (XTMPSi) in a similar way mentioned above for the film prepared from TMPSi-aqueous solution.

Water contact angle measurements

Static water contact angle (WCA) was measured at ambient temperature using 4-6 µL droplets of deionized water by gently depositing it on the substrate using a microsyringe. For CAH, the advancing and receding contact angles were measured at the front and back of the droplet moving along the tilted surface, respectively. The tilting angle measurements were performed using a mechanical level goniometer. All the measurements were repeated three times in different positions. The images were captured using a digital video camera and analyzed for contact angle measurements using SurfTens 3.0 software.

Characterization of the surface morphology

Surface morphologies of the films were mainly observed under scanning electron microscopy (SEM) (Jeol JSM 6060) using an electron acceleration between 5 and 10 kV. Profilometer measurements were carried

out by using a profilometer Ambios XP-2 with a stylus of 2.5 nm radius. The arithmetic mean of the surface roughness (R_a) was calculated from the roughness profile and finally the RMS (root mean squared) roughness was used.

Near edge X-ray absorption fine structure

NEXAFS experiments were carried out at the Brazilian Synchrotron Light Source (LNLS), Campinas, Brazil. The SGM (spherical grating monochromator) beam line, for ultraviolet and soft X-ray spectroscopy (250-1000 eV), which gives a spectral resolution ($E/\Delta E$) better than 2000, was used as the monochromatic photon source. The experimental set up includes a XYZ sample manipulator housed in an ultra high vacuum (UHV) chamber with a base pressure of 10^{-7} Pa. The stainless steel substrates were directly attached to the sample holder by using conducting double sided tape. No sample charging was observed throughout the experiments. NEXAFS spectra were obtained by measuring the total electron yield (electron current at the sample) simultaneously with a photon flux monitor (Au grid). The final data were normalized by this flux spectrum to correct for fluctuations in the beam intensity. NEXAFS spectral fittings were carried out using the BGAUSS multiline fitting program (BGAUSS, version 3.05., Tolmar Instrument, Hamilton, Ontario, Canada). Spectra were analyzed by first subtracting the pre-edge linear baseline. Height, position and width of the Gaussian and arctan functions were all allowed to be varied, within the limits, in the minimization algorithm.

FTIR-ATR analysis

Fourier transform infrared spectroscopy in attenuated total reflectance mode was used, (Alpha-P model, Bruker) the spectra of the casted films were obtained with spectral resolution of 4 cm⁻¹.

Results and Discussion

The wetting behaviors of ATMPSi and XTMPSi surfaces were first investigated by WCA measurements. As water droplet was deposited on their surfaces, high static WCA of $159 \pm 2^\circ$ and $160 \pm 2^\circ$ were observed for ATMPSi and XTMPSi surfaces, respectively. SEM images illustrate that the surfaces of ATMPSi (Figure 1) and XTMPSi (Figure 2) have heterogeneous rough surfaces with hierarchical micro and nanostructures.

When comparing WCA and CAH of ATMPSi and XTMPSi surfaces, the WCA values were similar but the samples showed a high difference in CAH. The maximum

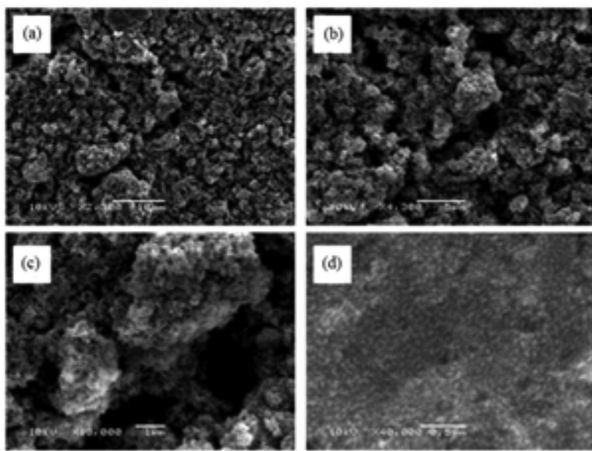


Figure 1. SEM images of ATMPsi film. WCA = $159 \pm 2^\circ$; CAH = 29° .

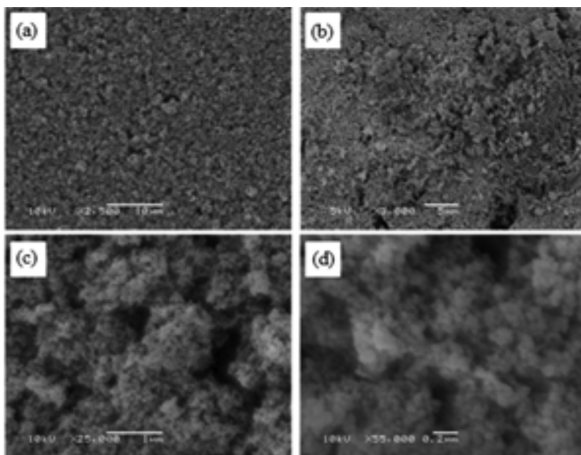


Figure 2. SEM images of XTMPSi film. WCA = $160 \pm 2^\circ$; CAH = 10° .

CAH of the XTMPSi surface was 10° , and on the contrary, CAH of the ATMPsi surface was 29° .²⁹ Nature shows examples with similar properties, such as in rose (*Rosa, cv. Bairage*) petals.³⁰ The static WCA of fresh and dried rose petals showed similar WCA (152° and 150° , respectively) but their CAH difference is very high. The difference in CAH of the fresh and dried states of rose petal was due to difference in the pitch values of the microstructure which changed because of the drying.²² In spite, SEM images (Figure 1) reveal a different surface morphology in ATMPsi film than XTMPSi film with different sizes of hierarchical micro and nanostructures, our previous studies showed that SEM and profilometer data cannot give a clear explanation of the obtained results on hysteresis. In that work, XPS technique was used to study the surface composition of superhydrophobic surface,²⁹ now NEXAFS was used to probe the surface chemical composition of superhydrophobic surface.

The Ti 2p NEXAFS spectra of TiO₂-P25, ATMPsi and XTMPSi are shown in Figure 3. The presence of two doublets arises from the spin-orbit interaction of the Ti 2p

core level, which splits the core level into a lower and higher energy level, $2p_{3/2}$ and $2p_{1/2}$, respectively. The two doublets found in the spectrum originate from an electron transfer from the Ti $2p_{3/2}$ and $2p_{1/2}$ levels to the Ti 3d orbitals in titanium dioxide, which split into t_{2g} and e_g orbitals in the octahedral symmetry.^{30,31} The size of the edge jump in NEXAFS spectra contains valuable information related to the number of absorbing atoms and it is useful for the study of surface coverage of chemisorbed molecules which vary with coverage.^{26,32} The size of the edge jump for t_{2g} and e_g of XTMPSi is less when compared to ATMPsi and TiO₂-P25. The decrease in the edge jump observed in the Ti $2p_{3/2}$ and Ti $2p_{1/2}$ transition intensity in XTMPSi can be explained by a more efficient coverage of TMPSi on the XTMPSi film compared to ATMPsi film. It is necessary to take into account that the edge jump information shown in Figure 3 is qualitative due to the different morphologies of the ATMPsi and XTMPSi films which can affect the NEXAFS intensity in the electron yield mode.

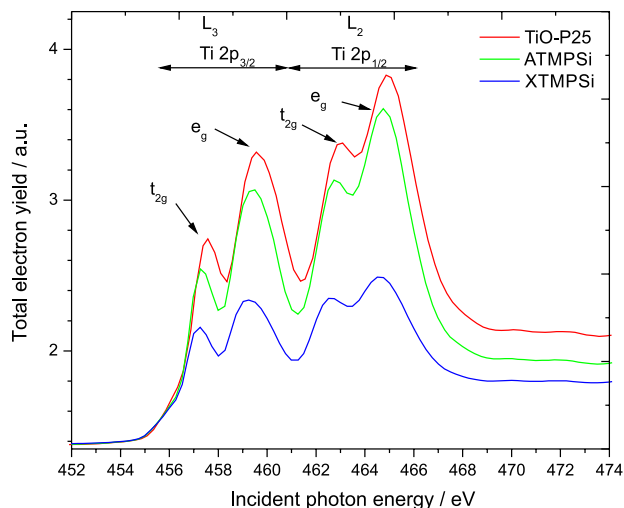
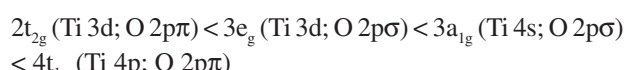


Figure 3. Ti 2p L-edge NEXAFS spectra of TiO₂-P25, ATMPsi and XTMPSi films.

The O 1s NEXAFS spectra of TiO₂-P25 and ATMPsi and XTMPSi are shown in Figure 4. The general trend in the oxygen K-edge features was initially interpreted using an empirical symmetry determined by the molecular orbital model, which involves the transition of one electron from the O 1s orbital to the various partially occupied and unoccupied molecular orbitals of metal oxides.^{33,34}

TiO₂ has octahedral symmetry with four types of well-defined molecular orbitals. The molecular orbitals and the corresponding atomic orbitals that contribute dominantly to the molecular orbitals of TiO₂ are in the energetic order.^{35,36}



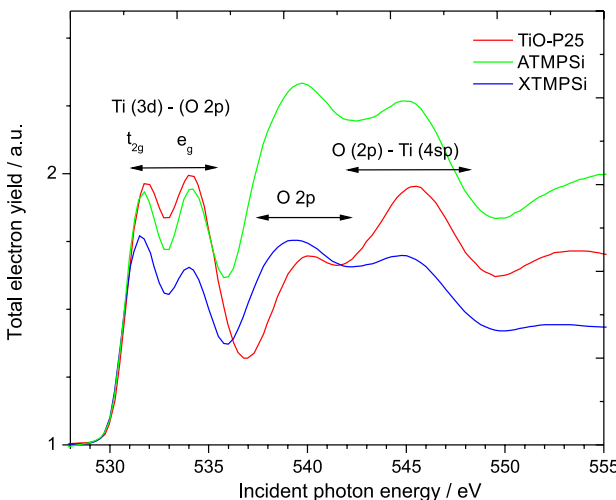


Figure 4. O K-edge NEXAFS spectra of TiO_2 -P25 powder, ATMPsi and XTMPSi films.

The transitions of O 1s electron to all four molecular orbitals of TiO_2 are dipole allowed because of the presence of p-character in these hybridized orbitals. All the four hybridized orbitals are completely empty due to the absence of 3d electrons in TiO_2 . The four O K-edge features can be assigned to the one electron transition from the O 1s orbital to the $2t_{2g}$, $3e_g$, $3a_{1g}$ and $4t_{1u}$ orbitals of TiO_2 , respectively. In Figure 4, the O K-edge features of TiO_2 -P25, ATMPsi and XTMPSi films were characterized by two relatively sharp features near the absorption edge followed by two broad resonances at higher energies. The first two peaks in each spectrum are related to the electron transfer of O 1s orbital to the hybridized orbitals of the O 2p + Ti 3d states, which are split into t_{2g} and e_g orbitals in the octahedral symmetry, respectively. The features corresponding to the transition of O 1s electron to $2t_{2g}$ and e_g are well resolved due to zero d electrons in TiO_2 which avoids the complication of the d electrons interaction effects.³⁷ The titanium e_g (d_z^2 , $d_{x^2-y^2}$) orbitals point directly towards the oxygen ligands, resulting in a strong overlap with the oxygen p_z orbital to form σ -type bonds. On the other hand, the metal t_{2g} (d_{xy} , d_{yz} , d_{zx}) orbitals are not directed towards the oxygen ligands, leading to the formation of π -type bonding, resulting in an energy hierarchy of $1t_{2g} > 2e_g$ in the bonding orbitals. Consequently, the energy positions of the corresponding antibonding orbitals should be reversed, as indicated by the energy hierarchy of $2t_{2g} < 3e_g$. The peak position at 531.9 and 534.0 eV are assigned to the $2t_{2g}$ and $3e_g$ orbital of TiO_2 -P25, respectively, and this spectral region is very sensitive to the local symmetry and ligand coordination.³⁸ The size of the edge jump in Figure 4 also clearly shows that there is a difference in the coverage of silane on the surface of TiO_2 films. The size of the edge jump for t_{2g} and e_g of XTMPSi is less when compared to ATMPsi and

TiO_2 -P25. TMPSi on the surface of the XTMPSi film covered the titanium dioxide particles well when compared to ATMPsi and TiO_2 -P25 decreasing the O 1s to Ti 3d transition intensity in XTMPSi.

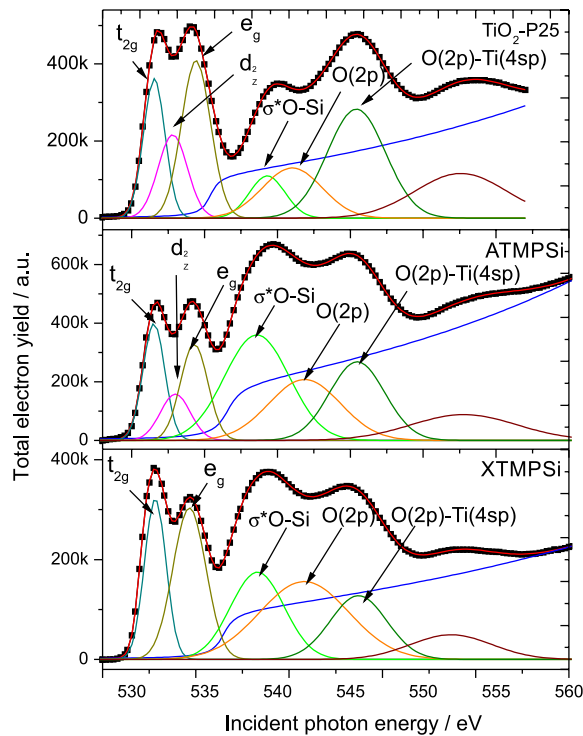
In Figure 4, the broad O K-edge features at higher energy just above the e_g orbital of 3d band in TiO_2 -P25 are dominated by oxygen p-character with little partial contribution of titanium 4sp states. Hence, the related peak in the O 1s spectrum is assigned to electron transfer of O 1s orbital to antibonding of oxygen 2p states. The last broad peak of O 1s spectrum in TiO_2 -P25 is related to the electron transfer of O 1s orbital to hybridized orbitals of the oxygen 2p and Ti 4sp states. These two features between 540.0 and 545.5 eV are due to the covalent mixing of O 2p and Ti 4sp states and are sensitive to the long-range order. The dip between the two peaks e_g and antibonding of O 2p state for ATMPsi and XTMPSi shifted to lower energy when compared to TiO_2 -P25. The shift in the dip to lower energy indicates that there is a change in the long-range order.

To confirm the change in the long-range order, the NEXAFS spectrum of oxygen K-edge was fitted using BGAUSS multiline fitting program, after correcting the background signal by normalizing the signals of the sample with the gold reference grid. The NEXAFS spectra are then fitted with Gaussian curves to correspond to the spectral features and an arctan function was used to model the ionization edge of the samples. The inflection point of the arctan function step was fixed at 536.8 eV. The NEXAFS spectra are then fitted with seven Gaussian peaks. The fit parameters used for TiO_2 -P25, ATMPsi and XTMPSi are shown in Table 1 and the fitted O 1s NEXAFS spectra were shown in Figure 5.

The shift in the dip between the two peaks e_g and antibonding of O 2p state for ATMPsi and XTMPSi was due to the rising up of a new peak at 538.5 eV. The peak at 538.5 eV corresponds to the transition of O 1s electron to σ^* O–Si bond which was in close agreement with the value 538.4 eV for the O 1s $\rightarrow \sigma^*$ O–Si transition of vinyltriethoxy silane.³⁹ A weaker signal of the same transition in the TiO_2 -P25 original sample provided by Degussa Corporation was also observed. In our previous investigation using XPS spectroscopy,²⁹ Ti–O–Si signal was also detected in the commercial sample indicating the addition of some silane additives on the TiO_2 -P25. The intensity and FWHM (full width half maximum) of this transition peak for ATMPsi were much higher than for XTMPSi. The higher intensity and FWHM of the σ^* O–Si transition of ATMPsi film indicate that there is more O–Si bond on the surface and high degree of overlap of O–Si bond in ATMPsi. The concentration of silane on ATMPsi and XTMPSi was different due to the solvent

Table 1. Fit parameters used for curve fitting in the O 1s NEXAFS spectra of TiO₂-P25, ATMPsi and XTMPSi

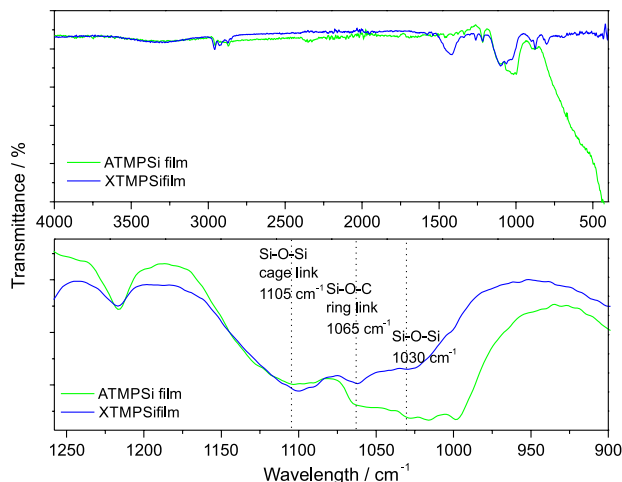
Orbital	TiO ₂ -P25		ATMPsi		XTMPSi	
	Peak / eV	FWHM / eV	Peak / eV	FWHM / eV	Peak / eV	FWHM / eV
t _{2g} (d _{xy} , d _{yz} , d _{zx})	531.5	1.7	531.5	1.8	531.5	1.8
d _z ²	532.7	2.4	532.9	2.4	—	—
e _g	534.5	2.4	534.2	2.2	534.0	2.7
σ*O-Si	539.3	2.9	538.5	5.2	538.5	4.3
O(2p)	541.0	4.8	541.8	5.8	541.8	7.2
O(2p)-Ti(4sp)	545.5	4.7	545.5	4.5	545.5	4.6
	552.5	7.4	552.8	8.5	552.1	6.6

**Figure 5.** NEXAFS O 1s curve fitted spectra of TiO₂-P25, ATMPsi and XTMPSi film samples.

effects and more amounts of silane were present on ATMPsi when compared to XTMPSi.

To further support the results, FTIR-ATR spectra were taken on ATMPsi and on XTMPSi. The relative intensities for the Si–O–Si bonding in cage link⁴⁰ at 1150 cm⁻¹ are almost the same for ATMPsi and XTMPSi (see Figure 6). On the contrary, for ATMPsi, the relative intensity peaks related to the Si–O–C in ring link⁴¹ at 1065 cm⁻¹ and Si–O–Si linkage at 1030 cm⁻¹ showed very strong increase in intensity when compared to XTMPSi. This shows that the concentration of Si–O–Si bonding (siloxanes) is high on the surface of ATMPsi and is mainly in the form of ring link structure due to hydrolysis and condensation reaction of TMPSi in TMPSi-aqueous solution. The

TMPSi-aqueous solution used for preparing ATMPsi film has oligomeric siloxanes formed during aging⁴² and there is no free or very few TMPSi monomers in the TMPSi-aqueous solution. These oligomeric siloxanes migrate to the surface due to difference in surface tension with aqueous solvent during casting of ATMPsi with titanium dioxide. In ATMPsi, there was a decline in the coverage of titanium dioxide particles due to formation of oligomeric siloxanes in TMPSi-aqueous solvent. This was confirmed by the board intensity band at 700 cm⁻¹ corresponding to Ti–O–Ti stretching of titanium dioxide. It would also indicate more free TiO₂ in the ATMPsi film with higher Ti–OH concentration, confirming previous XPS studies.²⁹ The higher CAH of the ATMPsi surface is due to the polar interaction between the uncovered hydroxyl groups of titanium dioxide particles and the water droplet. The hydroxyl groups are formed on titanium dioxide surface of ATMPsi due to water adsorption⁴³ during stirring with aqueous solvent.

**Figure 6.** FTIR-ATR spectra of ATMPsi and XTMPSi films.

On the other hand, for XTMPSi, the relative intensities at bonding mode 1105 cm⁻¹ correspond to Si–O–C in open

link showed a little increase in intensity when compared to ATMPsi. This happened because in TMPSi-xylene solvent there was no possibility for hydrolysis and all the TMPSi remains as monomers. These silane monomers in xylene solvent cover the titanium dioxide particles by bonding with hydroxyl group of the titanium dioxide and undergo polycondensation reaction during casting of XTMPSi. The polycondensation reaction forms Si–O–Si linkage in open link and completely covered the titanium dioxide which is confirmed by the disappearance of titanium dioxide peak in Figure 6 and appeared a band between 1495 and 1463 cm⁻¹ due to xylene absorbed by titanium dioxide particles while stirring with TMPSi-xylene solution. The uncovered hydroxyl groups of titanium dioxide act as active sites for xylene adsorption during stirring with TMPSi-xylene solvent and the absorbed xylene covered the sites of exposed titanium cations with unsaturated coordination. Due to complete coverage of titanium dioxide by TMPSi and xylene, CAH of XTMPSi is much lower than ATMPsi.

Our results show that it is necessary to take into account the actual chemistry at the surface after the treatments and not only the complex hierarchical micro-nanostructure. In many cases, it is considered only that by optimization of the hierarchical structure and the geometrical design a superhydrophobic surface can be produced.^{44,45} In particular, properties such as CAH seem to be important, for example, in the ice adhesion strength on rough hydrophobic surface. Our group showed in a previous publication²⁹ and clearly in the present work that chemical heterogeneity of the surface can strongly affect the dynamic of the wetting phenomena without altering the static component of the superhydrophobicity. By using NEXAFS and FTIR-ATR spectroscopy, it was possible to explain the difference in surfaces having the same static water CA, but different CAH.

Conclusions

The superhydrophobic surfaces fabricated using aqueous solvent (ATMPsi: WCA = 159 ± 2° and CAH = 29°) and non-aqueous solvent (XTMPSi: WCA = 160 ± 2° and a maximum CAH = 10°) were probed in detail by NEXAFS and FTIR-ATR spectroscopies. The NEXAFS O 1s spectra reveal that the concentrations of silanes on ATMPsi and XTMPSi were different due to the solvent effects and more amounts of silane were present on ATMPsi than XTMPSi. This is confirmed by the higher intensity and FWHM of the σ* O–Si transition of ATMPsi film. Additionally, the higher decrease in the edge jump observed on the Ti 2p_{3/2} signal of XTMPSi film confirmed a better coverage of the TiO₂ nanoparticles by TMPSi than the ATMPsi film.

The FTIR-ATR analysis of superhydrophobic surfaces confirmed that there are more siloxanes on the surface of ATMPsi than XTMPSi. This is due to the oligomeric siloxanes formed during aging in TMPSi-aqueous solution. The formation of oligomeric siloxanes hinders the complete coverage of the titanium dioxide particles and results in higher hysteresis in ATMPsi. For XTMPSi, the TMPSi monomers in non-aqueous solvent completely cover the titanium dioxide particles and result in lower hysteresis. The present work highlights the importance of chemical heterogeneity of the surface on the final properties of a superhydrophobic surface by modifying the dynamic of the wetting phenomena without altering the static component of the superhydrophobicity.

Acknowledgments

This work was partially supported by the Conselho Nacional de Desenvolvimento Científico e Tecnológico (CNPq), process No. 550461/2012-4, FAPERGS/CNPq (10/0050-6) (Brazil) and the National Synchrotron Light Laboratory (LNLS, Brazil). The authors would also like to acknowledge the technical assistance of the Accelerator Group, especially the VUV and the Soft X-ray spectroscopy Group. We thank the Microscopy and Microanalyses Center (CME), UFRGS for the SEM analysis. The author R. R., recipient of a TWAS-CNPq fellowship, thanks them for financial support.

References

1. Barthlott, W.; Neinhuis, C.; *Planta* **1997**, 202, 1.
2. Nakajima, A.; Hashimoto, K.; Watanabe, T.; Takai, K.; Yamauchi, G.; Fujishima, A.; *Langmuir* **2000**, 16, 7044.
3. Lai, Y.; Lin, C.; Huang, J.; Zhuang, H.; Sun, L.; Nguyen, T.; *Langmuir* **2008**, 24, 3867.
4. Hou, W.; Wang, Q.; *Langmuir* **2009**, 25, 6875.
5. Weibel, D. E.; Michels, A. F.; Feil, A. F.; Amaral, L.; Teixeira, S. R.; Horowitz, F.; *J. Phys. Chem. C* **2010**, 114, 13219.
6. Zhang, L.; Wu, J.; Wang, Y.; Long, Y.; Zhao, N.; Xu, J.; *J. Am. Chem. Soc.* **2012**, 134, 9879.
7. Yilgor, I.; Bilgin, S.; Isik, M.; Yilgor, E.; *Polymer* **2012**, 53, 1180.
8. Ruan, M.; Li, W.; Wang, B.; Luo, Q.; Ma, F.; Yu, Z.; *Appl. Surf. Sci.* **2012**, 258, 7031.
9. Wenzel, R. N.; *Ind. Eng. Chem.* **1936**, 28, 988.
10. Cassie, A. B. D.; Baxter, S.; *Trans. Faraday Soc.* **1944**, 40, 546.
11. Das, A.; Hayvaci, H. T.; Tiwari, M. K.; Bayer, I. S.; Erricolo, D.; Megaridis, C. M.; *J. Colloid Interface Sci.* **2011**, 353, 311.
12. Kako, T.; Nakajima, A.; Irie, H.; Kato, Z.; Uematsu, K.; Watanabe, T.; Hashimoto, K.; *J. Mater. Sci.* **2004**, 39, 547.

13. Patankar, N. A.; *Langmuir* **2004**, *20*, 7097.
14. Kwon, Y.; Patankar, N.; Choi, J.; Lee, J.; *Langmuir* **2009**, *25*, 6129.
15. Hong, X.; Gao, X.; Jiang, L.; *J. Am. Chem. Soc.* **2007**, *129*, 1478.
16. Wang, S.; Jiang, L.; *Adv. Mater.* **2007**, *19*, 3423.
17. Gao, L.; McCarthy, T. J.; *Langmuir* **2007**, *23*, 3762.
18. Panchagnula, M. V.; Vedantam, S.; *Langmuir* **2007**, *23*, 13242.
19. Marmur, A.; Bitton, E.; *Langmuir* **2009**, *25*, 1277.
20. Erbil, H. Y.; Cansoy, C. E.; *Langmuir* **2009**, *25*, 14135.
21. Feng, L.; Zhang, Y.; Xi, J.; Zhu, Y.; Wang, N.; Xia, F.; Jiang, L.; *Langmuir* **2008**, *24*, 4114.
22. Bhushan, B.; Her, E. K.; *Langmuir* **2011**, *26*, 8207.
23. Exrand, C. W.; *J. Colloid Interface Sci.* **1998**, *207*, 11.
24. Gao, L.; McCarthy, T. J.; *Langmuir* **2006**, *22*, 6234.
25. Stohr, J.; Samant, M. G.; *J. Electron Spectrosc. Relat. Phenom.* **1999**, *98-99*, 189.
26. Stöhr, J.; *NEXAFS Spectroscopy*; Springer-Verlag: Berlin/Heidelberg, Germany, 1992.
27. Krishnan, S.; Ayothi, R.; Hexemer, A.; Finlay, J. A.; Sohn, K. E.; Perry, R.; Ober, C. K.; Kramer, E. J.; Callow, M. E.; Callow, J. A.; Fischer, D. A.; *Langmuir* **2006**, *22*, 5075.
28. Unger, W. E. S.; Lippitz, A.; Woll, C.; Heckmann, W.; *Fresenius J. Anal. Chem.* **1997**, *358*, 89.
29. Rajajeyaganthan, R.; Weibel, D. E.; *Appl. Surf. Sci.* **2012**, *258*, 7950.
30. Soriano, L.; Abbate, M.; Vogel, J.; Fuggle, J. C.; Fernández, A.; González-Elipe, A. R.; Sacchi, M.; Sanz, J. M.; *Surf. Sci.* **1993**, *290*, 427.
31. van der Laan, G.; *Phys. Rev. B: Condens. Matter.* **1990**, *41*, 12366.
32. Born, M.; Wolf, E.; *Principles of Optics*; Pergamon: London, UK, 1959.
33. Grunes, L. A.; Leapman, R. D.; Wilker, C. N.; Hoffmann, R.; Kunz, A. B.; *Phys. Rev. B: Condens. Matter.* **1982**, *25*, 7157.
34. Fischer, D. W.; *J. Appl. Phys.* **1970**, *41*, 3561.
35. de Groot, F. M. F.; Grioni, M.; Fuggle, J. C.; Ghijssen, J.; Sawatzky, G. A.; Petersen, H.; *Phys. Rev. B: Condens. Matter.* **1989**, *40*, 5715.
36. Chen, J. G.; Fruhberger, B.; Colaianni, M. L.; *J. Vac. Sci. Technol., A* **1996**, *14*, 1668.
37. Lusvardi, V. S.; Barteau, M. A.; Chen, J. G.; Eng Jr., J.; Frühberger, B.; Teplyakov, A.; *Surf. Sci.* **1998**, *397*, 237.
38. de Groot, F. M. F.; Faber, J.; Michiels, J. J. M.; Czyzyk, M. T.; Abbatte, M.; Fuggle, J. C.; *Phys. Rev. B: Condens. Matter.* **1993**.
39. Tulumello, D.; Cooper, G.; Koprinarov, I.; Hitchcock, A. P.; Rightor, E. G.; Mitchell, G. E.; Rozeveld, S.; Meyers, G. F.; Stokich; *J. Phys. Chem. B* **2005**, *109*, 6343.
40. Chang, T. C.; Liu, P. T.; Mor, Y. S.; Sze, S. M.; Yang, Y. L.; Feng, M. S.; Pan, F. M.; Dai, B. T.; Chang, C. Y.; *J. Electrochem. Soc.* **1999**, *146*, 3802.
41. Bellamy, L. J.; *The Infrared Spectra of Complex Molecules*; Chapman and Hall Ltd.: London, UK, 1975.
42. Plueddemann, E. P.; *Silane Coupling Agents*; Plenum Publishing Corporation: New York, USA, 1982.
43. Koparde, V. N.; Cummings, P. T.; *J. Phys. Chem. C* **2007**, *111*, 6920.
44. Li, W.; Cui, X. S.; Fang, G. P.; *Langmuir* **2010**, *26*, 3194.
45. Henderson, M. A.; Epling, W. S.; Peden, C. H. F.; Perkins, C. L.; *J. Phys. Chem. B* **2003**, 534.

Submitted: February 17, 2013

Published online: June 4, 2013